8-21-2004

The Oxford-Dartmouth Thirty Degree Survey - I. Observations and Calibration of a Wide-Field Multiband Survey

Emily C. MacDonald
University of Oxford

Paul Allen
University of Oxford

Gavin Dalton
University of Oxford

Leonidas A. Moustakas
University of Oxford

Catherine Heymans
University of Oxford

See next page for additional authors

Mon. Not. R. Astron. Soc. **352,** 1255–1272 (2004) doi:10.1111/j.1365-2966.2004.08014.x

The Oxford–Dartmouth Thirty Degree Survey – I. Observations and calibration of a wide-field multiband survey

Emily C. MacDonald,[1⋆] Paul Allen,[1,2] Gavin Dalton,[1,3] Leonidas A. Moustakas,[1,4] Catherine Heymans,[1,5] Edward Edmondson,[1] Chris Blake,[6] Lee Clewley,[1] Molly C. Hammell,[7] Ed Olding,[1] Lance Miller,[1] Steve Rawlings,[1] Jasper Wall,[1] Gary Wegner[7] and Christian Wolf[1]

[1] *University of Oxford, Astrophysics, Keble Road, Oxford OX1 3RH*
[2] *Research School of Astronomy and Astrophysics, The Australian National University, Mount Stromlo Observatory, Cotter Rd, Weston, ACT 2611, Australia*
[3] *Space Science and Technology Division, Rutherford Appleton Laboratory, Didcot OX11 OQX*
[4] *Space Telescope Science Institute, 3700 San Martin Drive, Baltimore, MD 21218, USA*
[5] *Max-Planck-Institut für Astronomie, Königstuhl, D-69117 Heidelberg, Germany*
[6] *Institute for Astronomy, School of Physics A28, University of New South Wales, New South Wales 2006, Australia*
[7] *Dartmouth College, 6127 Wilder Laboratory, Hanover, NH 03755-3528, USA*

Accepted 2004 May 11. Received 2004 May 10; in original form 2004 March 3

ABSTRACT

The Oxford–Dartmouth Thirty Degree Survey (ODTS) is a deep, wide, multiband imaging survey designed to cover a total of 30 deg^2 in $BVRi'Z$, with a subset of U- and K-band data, in four separate fields of 5–10 deg^2 centred at 00:18:24 +34:52, 09:09:45 +40:50, 13:40:00 +02:30 and 16:39:30 +45:24. Observations have been made using the Wide Field Camera on the 2.5-m Isaac Newton Telescope (INT) in La Palma to average limiting depths (5σ Vega, aperture magnitudes) of $U = 24.8$, $B = 25.6$, $V = 25.0$, $R = 24.6$ and $i' = 23.5$, with observations taken in ideal conditions reaching the target depths of $U = 25.3$, $B = 26.2$, $V = 25.7$, $R = 25.4$ and $i' = 24.6$. The INT Z-band data were found to be severely effected by fringing and, consequently, are now being obtained at the MDM observatory in Arizona. A complementary K-band survey has also been carried out at MDM, reaching an average depth of $K_{5\sigma} \approx 18.5$. At present, approximately 23 deg^2 of the ODTS have been observed, with 3.5 deg^2 of the K-band survey completed. This paper details the survey goals, field selection, observation strategy and data reduction procedure, focusing on the photometric calibration and catalogue construction. Preliminary photometric redshifts have been obtained for a subsample of the objects with $R \leqslant 23$. These results are presented alongside a brief description of the photometric redshift determination technique used. The median redshift of the survey is estimated to be $z \approx 0.7$ from a combination of the ODTS photometric redshifts and comparison with the redshift distributions of other surveys. Finally, galaxy number counts for the ODTS are presented which are found to be in excellent agreement with previous studies.

Key words: catalogues – surveys – galaxies: general – cosmology: observations – large-scale structure of Universe.

1 INTRODUCTION

Understanding the origin and evolution of galaxies and large-scale structure within the Universe remains one of the most challenging areas in modern cosmology. With the completion of the 2-Degree Field Galaxy Redshift Survey (2dFGRS, Colless 2001) and the imminent conclusion of the Sloan Digital Sky Survey (SDSS, Stoughton et al. 2002), we are witnessing the emergence of an accurate and detailed model of structure in the nearby Universe. However, to gain insight into the evolution of the Universe out to higher redshifts requires the advent of deep surveys, with substantial areal coverage to ensure large number statistics and avoid cosmic variance. A number of such surveys have been initiated in recent years, each with individual goals but all hoping to shed light on the structure and formation of the high redshift Universe. For example, the ESO Imaging Survey (EIS, Nonino 1999) is a 24 deg^2 moderately deep I-band

⋆E-mail: ecm@astro.ox.ac.uk

survey ($I_{5\sigma\,\mathrm{AB}} \approx 23.7$) with additional limited coverage in *B*, *V* and the infrared. A subarea of the EIS (0.25 deg^2) is covered in *UBVRI* to $I_{5\sigma\,\mathrm{AB}} \approx 24.7$ forming the EIS-Deep survey (Arnouts et al. 2001). The Canada–France Deep Fields Survey (CFDF, McCracken et al. 2001), consists of four deep fields totalling 1 deg^2, all covered in *V* and *I* ($I_{5\sigma\,\mathrm{AB}} \approx 25.5$), with additional *U* and *B* coverage. Also ongoing are the Combo-17 survey (Wolf et al. 2003), where fields totalling ≈1 deg^2 have been observed through 17 medium-band filters to a limiting magnitude of $R_{5\sigma\,\mathrm{AB}} = 26.2$, and the NOAO Deep Wide-Field Survey (NDWFS, Jannuzi et al. 2002), which will cover 24 deg^2 in *BRIJH* and *K* to $R_{5\sigma\,\mathrm{AB}} = 26$. Here we describe the Oxford–Dartmouth Thirty Degree Survey (ODTS), which aims to provide multi band observations, to allow for the determination of photometric redshifts, to depths comparable with the deepest wide field surveys to date and over a wider area. The Wide Field Camera (WFC) on the Isaac Newton Telescope (INT) on la Palma has been used to observe 23 deg^2 (out of the total 30 deg^2) of *BVR* ($R_{5\sigma\,\mathrm{AB}} \approx 25.6$ assuming 1-arcsec seeing) and i' imaging, with a subset of *U*-band data. The *Z*-band data, although initially planned for observation at the INT, are now currently being acquired using the 2.4 m Hiltner Telescope at the MDM observatory, Kitt Peak (see Section 3.1). Also, a K-Band survey, designed to run in parallel with and be complementary to the optical ODTS, is currently being carried out using the 1.3 m McGraw-Hill Telescope at MDM, to a depth of K ≈18.5 (Olding 2002). In addition, deep radio data have been obtained from the VLA, covering a total of 2 deg^2 of the ODTS to a 5σ flux density limit of 100 μJy at 1.4 GHz with a resolution of 1.5 arcsec, and with deeper 1.4-GHz data and lower frequency (e.g. 74 and 330 MHz) radio data over some fraction of the area. Part of the ODTS data also overlaps with the Texas–Oxford One Thousand (TOOT) redshift survey of radio sources (Hill & Rawlings 2003), allowing us to obtain spectroscopic redshift measurements for a number of sources in the ODTS.

The ODTS was initially designed with the following goals.

(i) Clustering of bright Lyman break galaxies (LBGs, Allen et al., submitted). Lyman Break Galaxies exhibit a break in their spectra shortwards of the Lyman limit, 912 Å in the rest frame. For LBGs at high redshift, $z = 3$ and 4, this results in a *U*- and *B*-band drop out thus permitting the detection of Lyman Break candidates using the ODTS multi band data. As a result of the extent of the ODTS, the clustering of LBGs can be studied over a much larger area than previously available, thus minimizing the effects of cosmic variance.

(ii) Clustering properties of faint galaxies (MacDonald et al., in preparation). Previous surveys have lacked the combination of both depth and width required to explore the large-scale clustering and evolution of faint galaxies as a function of magnitude, colour and redshift. The size of the ODTS potentially allows the measurement of the angular correlation function up to degree scales.

(iii) Clustering of extremely red objects (EROs, Olding 2002). Matching the ODTS *R*-band data with the MDM *K*-band data will allow for the selection of a large number of EROs, the criteria being an $R - K > 5$, over a relatively large area. The ODTS can be used to estimate their space density and photometric redshifts will allow for clustering and evolution to be analysed.

(iv) Detection of high redshift ($z > 5$) quasars. Extremely high redshift quasi-stellar objects (QSOs) are rare but known to exist, as confirmed by the SDSS (Anderson et al. 2001). Uncertainties still surround issues such as the shape of their luminosity function at the faint end and their evolution at high redshift. Colour selection methods, via the (*V*–*i*) versus (*i*–*Z*) colour–colour relation, will allow for the selection of faint QSOs at $z > 5$.

(v) High redshift galaxy clusters. Combining information concerning the cluster colour–magnitude relation (Gladders & Yee 2000) with photometric redshifts and a search for spatial overdensities, clusters with $0.2 < z < 1.2$ can be selected from the ODTS. The aim is to use this sample to investigate the cluster colour–magnitude relation as a function of redshift and cluster mass (Hammell et al., in preparation).

This paper summarizes the ODTS and presents a full description and characterization of the survey data, structured as follows. Section 2 discusses the survey design, specifically the criteria adopted for the field selection, the filter set used, and the observation strategy. Section 3 outlines the basic data reduction process. Section 4 describes the photometry and source extraction, and Section 5 outlines the astrometry. Section 6 details the photometric calibration for each band and Section 7 outlines the algorithm used to generate the final matched catalogue. In Section 8 a brief summary of the photometric redshift determination is given and in Section 9 galaxy number counts are presented and compared with previous studies. Finally, a summary is given in Section 10.

2 THE OXFORD–DARTMOUTH THIRTY DEGREE SURVEY DESIGN

The ODTS was initiated in 1998 August, and was designed to make use of the Wide Field Camera located at the prime focus of the 2.5-m Isaac Newton Telescope on La Palma. It is a deep-wide survey facilitating six filters per field; namely RGO *U*, Kitt Peak *B*, Harris *V*, Harris or Sloan *R*, Sloan i' and RGO *Z*, the system response for which are provided in Fig. 1. Six filters were selected to allow for the determination of photometric redshifts for objects in the survey. In particular, the Kitt Peak *B* and Sloan–Gunn i' filters were adopted, as opposed to their Johnson–Cousins counterparts, because they have higher throughput and simpler, more box-like transmission curves which are better for photometric redshift determination and allow for cleaner colour–colour selection of objects with sensitive spectral features, such as LBGs. In addition the i'

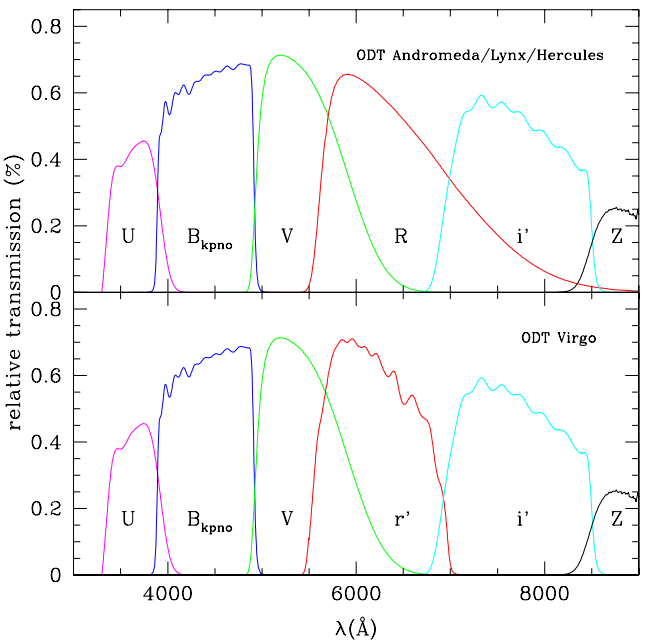

Figure 1. The system response, determined from the filter transmission curves and the CCD response, for the full set of ODTS filters (*UBVRi'Z*).

Table 1. Field centres for the ODT survey in equatorial and Galactic coordinates.

Field	α(J2000)	δ(J2000)	l	b
Andromeda	00 18 24	+34 52 00	115	−27
Lynx	09 09 45	+40 50 00	181	+42
Hercules	16 39 30	+45 24 00	70	+41
Virgo	13 40 00	+02 30 00	330	+62

Table 2. The exposure times and expected detection limits (5σ aperture Vega and AB magnitudes) for the various passbands used for the ODTS. With the exception of the *U* and *Z* images, each pointing is segregated into three separate exposures with 5-arcsec offsets of the telescope.

Filter	Exposure time (s)	5σ Limiting depths using 2-arcsec aperture AB magnitudes	Vega magnitudes
U	6 × 1200	26.1	25.3
B	3 × 900	26.1	26.2
V	3 × 1000	25.7	25.7
R	3 × 1200	25.6	25.4
i'	3 × 1100	25.0	24.6
Z	1 × 600	22.4	21.9

filter is less susceptible to fringing caused by sky emission lines (see Section 3.1). Initially the Sloan–Gunn r' filter was not available at the INT, so observations were made using the Harris *R* filter which has a long red tail, and so suffers from notable fringing. However, the r' filter became available at the beginning of the Virgo field (see Table 1) observations and, consequently, was adopted for this field only. Initially, the ODTS was designed to cover ∼30 deg^2 to estimated depths (2-arcsec aperture Vega magnitudes) of $B = 26.2$, $V = 25.7$, $R = 25.4$ and $i' = 24.6$ and $Z = 22.0$, assuming a 5σ detection threshold and the median INT seeing of 1 arcsec, with an additional subarea of ≈5 deg^2 in $U(= 25.3)$ assuming ideal (seeing <0.7 arcsec) conditions. The initial Vega and AB magnitude limits for the survey are given in Table 2.

2.1 Field selection

Initially the Andromeda, Hercules and Lynx fields were chosen from a number of potential fields primarily for their observability during the first few allocated INT runs; their centres are shown in Table 1. The Virgo field was added at a later date to optimize year round observability and provide a field visible from the Southern hemisphere. In addition, the selected fields had to have low extinction, overlap with existing (multiwavelength) data sets and have a lack of bright stars, nearby galaxies and bright, large clusters. The mean extinction, $E(B - V)$, in each field was determined from the DIRBE corrected IRAS 100 μm maps of Schlegel, Finkbeiner & Davis (1998) and was found to be <0.06 in Andromeda and <0.02 in the remaining fields. The large (4-arcmin) pixel scale of the *IRAS* maps provides little information concerning the small-scale distribution of the Galactic dust, and therefore making extinction corrections using 4-arcmin cells, as opposed to individual galaxy corrections, could imprint a low level spurious clustering pattern. This potential bias combined with the low galactic extinction values meant no extinction corrections for galactic dust were applied.

2.2 Observations

Observations were made over 63 nights between 1998 August and 2003 March, during which time several nights were lost, due in part to instrument problems, but mostly due to bad weather conditions. The data were obtained using the WFC which is a mosaic of four 4096 × 2048 pixel charge-coupled device (CCD) chips, each chip covering of 22.8 × 11.4 arcmin^2 (≈0.29 deg^2 per WFC pointing) with a pixel scale of 0.33 arcsec pixel^{-1}. At the beginning and end of each night bias, dark and twilight flat-field frames were acquired. Landolt standard star frames were also observed several times throughout each night (see Section 4.1). On the whole, data were taken when conditions were either photometric or light cirrus was present, with variable seeing across the fields. Assuming the median INT seeing of 1 arcsec the 5σ depths shown in Table 2 implied a total of 3.7 h per pointing were required to obtain the multi band data ($BVRi'Z$), resulting in a survey speed of ∼1.2 deg^2 per night (not including the *U* data). The median seeing values actually obtained for each field in each band are presented in Table 3 alongside the median depth reached in each band in each field. There are no values for the *Z*-band data at present because the fringing proved too severe (see Section 3.1). Fig. 2 illustrates how the *R*-band depths vary across the Andromeda field (fully reduced data only) and Fig. 3 shows the corresponding cumulative distribution of fraction of total area versus depth in *R*.

Table 3. Median seeing and median depths reached (Vega magnitudes) for the reduced field data, where the depth of each frame has been determined from the turn over in number counts.

	Andromeda		Lynx		Hercules	
Filter	seeing	depth	seeing	depth	seeing	depth
U	1.00	24.8	n/a		n/a	
B	1.31	25.3	1.46	25.61	1.24	25.8
V	1.24	24.8	1.23	25.2	1.66	24.9
R	1.13	24.3	1.36	24.7	1.32	24.7
i'	1.10	23.4	1.55	23.7	1.64	23.5

In order to cover each of the ODTS fields efficiently with the WFC focal plane geometry, a tiling pattern involving using the camera in two rotational positions, 180° apart, was employed. The fields were covered by a diagonal grid, with the rotation alternating with each row. Each grid element, representing one pointing of the INT WFC, was assigned a unique ODTS identification number. Fig. 4 depicts the subfields (i.e. the WFC camera pointings), where the coloured bands within the grid elements indicate which filters each of the subfields have been observed in thus far. A couple of WFC pointings have been highlighted for clarity in Fig. 4(c) and the WFC chips have been labelled. In this paper, the terminology *pointing* refers to one entire WFC image and *frame* refers to one chip of the WFC.

Observations for the optical (INT) portion of the ODTS were completed in 2003 March with approximately 23 deg^2 of the survey observed in $BVRi'$, although the data reduction is still ongoing. The *U* data, taken in the best observing conditions, currently cover ∼1 deg^2 in the Andromeda field. The total coverage of the fully reduced data is summarized in Table 4.

3 DATA REDUCTION

3.1 Preprocessing

Standard IRAF[1] data reduction routines were implemented to remove the instrumental signature. Bias subtraction was made using the

[1] IRAF is distributed by the NOAO, which is operated by the Association of Universities for Research in Astronomy, Inc. under cooperative agreement with the National Science Foundation.

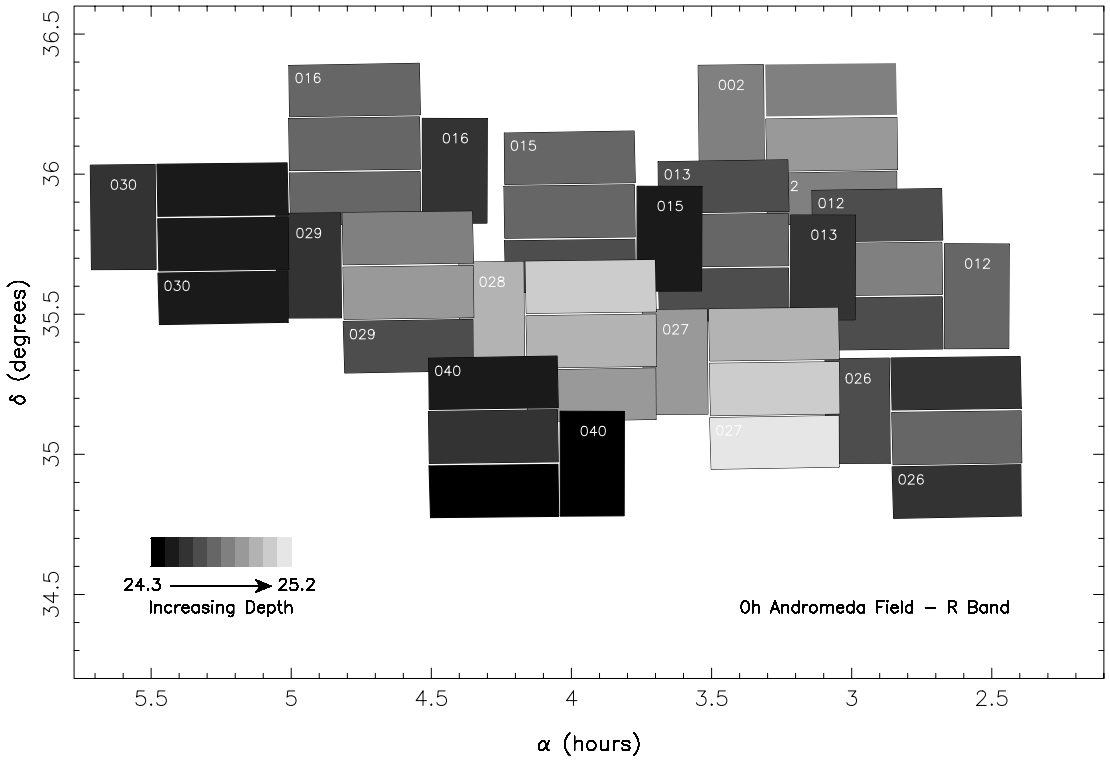

Figure 2. A grey-scale image of the reduced *R*-band Andromeda data (totalling 2.78 deg^2), demonstrating how the depths reached vary across the field. Frame depths vary from 24.3 to 25.2 mag where the lighter the shade, the greater the depth. Variable conditions and individual chip response differences lead to slight changes of depth within each pointing as expected. It should be noted that there are small gaps (≈1 arcmin) present between the WFC chips.

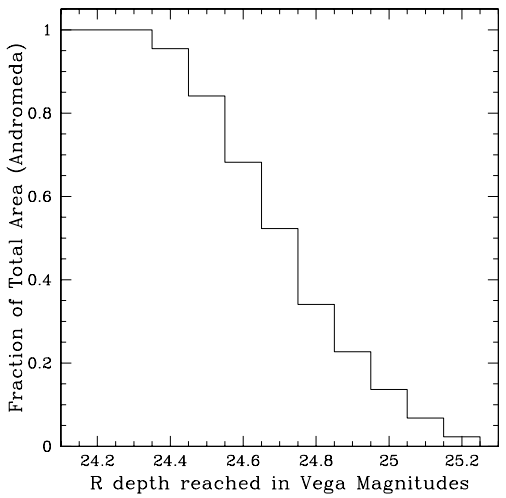

Figure 3. The cumulative distribution of the fraction of area (totalling 2.78 deg^2) versus *R* depth reached for the reduced Andromeda data. Frame depths vary from 24.3 to 25.2.

chip overscan regions and master bias frames. The dark current was found to be negligible. Small non-linearities were known to exist in the WFC chips, the corrections for which were determined by the Cambridge Astronomical Survey Unit[2] and were applied appropriate to the time of observation.

[2] The values of the linearity corrections used, along with other information concerning the INT WFC, are available on the CASU website, http://www.ast.cam.ac.uk/∼wfcsur/index.php.

Corrections for variations in the pixel to pixel sensitivity and vignetting caused within the optics were made by dividing frames by the appropriate master flat-field, created by median combining the object frames, or the twilight flat frames in the case of those bands subject to fringing. On comparison of the *B*- and *V*-band twilight flats with the deep sky flats obtained from the *B* and *V* object frames, it was found that no illumination correction was necessary.

The *R*-, *i*′- and *Z*-band images were found to suffer from fringing caused by the multiple reflection and interference of the night-sky emission lines within the CCD. Unfortunately, defringing is far from trivial as the relative intensities of the emission lines are dependent on the atmospheric conditions, thus fringing is a time varying effect. To defringe the data the bias corrected, flat-fielded *R*, *i*′ and *Z* target frames from each night were median combined. This resulted in master fringe frames for each band, containing the residual sky fringe pattern. For each image, the master fringe frame was subtracted, scaling the fringe level of the master fringe frame to that of the fringing in the images. This effectively removes the dominant zeroth-order fringing component, an example of which can be seen in Fig. 5.

For the WFC images, fringing effects were found to be ∼0.5 per cent of the sky level for the *R* band, ∼3 per cent for *i*′ and ∼6 per cent for *Z*. After the defringing process the residual fringing level was reduced to <0.1 per cent of the sky but the *Z*-band fringing remained visible at ∼0.5 per cent. Consequently, the acquisition of *Z*-band data using the INT had to be abandoned. *Z* data for all observed ODTS fields are now being obtained using the 8k camera on the 2.4 m Hiltner telescope at MDM (3 × 1200 s exposures). This camera has thick CCDs and produces much cleaner *Z*-band imaging.

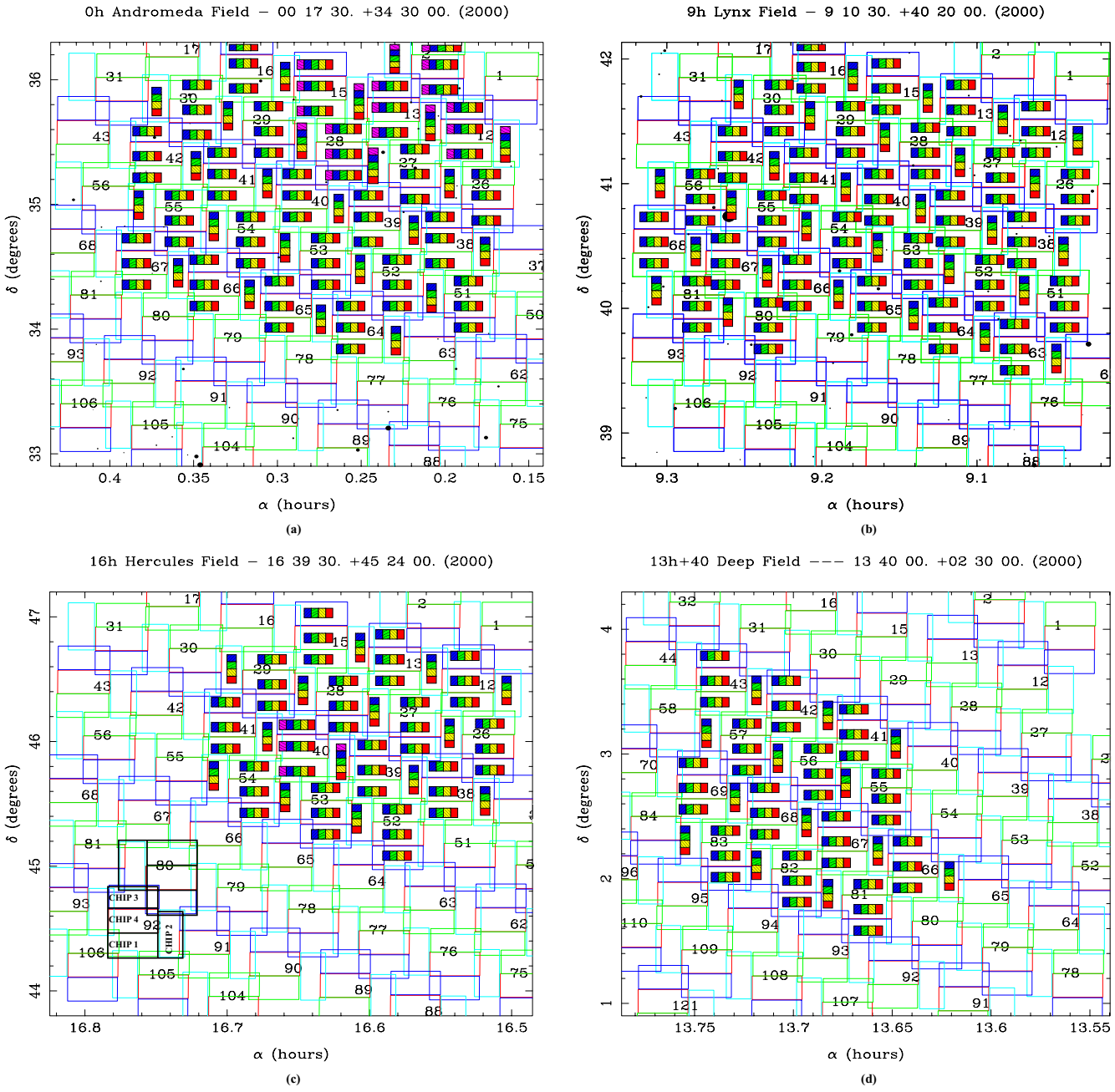

Figure 4. The (a) 0-h Andromeda, (b) 9-h Lynx, (c) 16-h Hercules and (d) 13-h Virgo fields divided into diagonal grids, where each numbered grid element represents one WFC pointing. The four individual chips of the WFC can be seen and in the bottom left corner of diagram (c) two of the WFC pointings are outlined in black for clarity, and the chip numbers have been marked. Coloured coded bars illustrate the coverage of each subfield to date.

Table 4. Current areas of observed and reduced multiband ($UBVRi'$) data for the four ODTS fields.

	Area in deg^2, observed/reduced				
Field	U	B	V	R	i'
And	1.16/1.16	6.96/2.31	6.96/2.58	6.96/2.78	6.96/2.81
Lynx	n/a	7.83/1.79	7.83/1.77	7.83/1.78	7.83/1.79
Herc	0.29/0	4.06/1.33	4.06/1.75	4.06/1.30	4.06/1.33
Virgo	n/a	3.77/0	3.77/0	3.77/0	3.77/0

Bad pixel masks were then created for each chip and the defective pixels were effectively removed by interpolating across them in each image.

For each pointing in $BVRi'$ three images were taken, offset from each other by 5 arcsec to ensure that different areas of the sky fell on the bad detector regions. The U-band data required six pointings to reach the required depth so these were taken in two groups of three, offsetting in each group as for the other bands. These were then aligned, median combined and trimmed, where the median combination was performed using the IRAF average sigma clipping

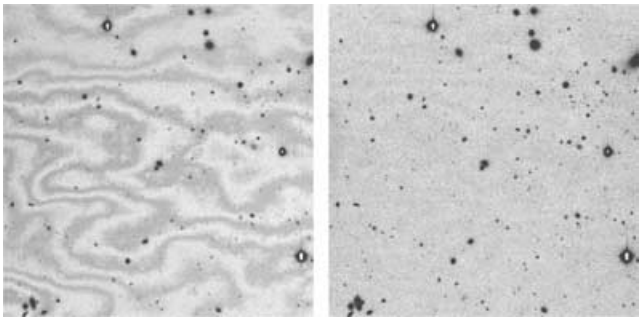

Figure 5. A subsection of an i' image before (left) and after (right) undergoing defringing.

algorithm, rejecting values deviating from the mean by $> \pm 3\sigma$ to ensure the removal of any remaining bad pixels and cosmic rays.

To obtain the correct flux measurement for each of the sources the contribution from the sky background also had to be considered. On initial reduction of the ODTS data, significant sky gradients were found across some images which SEXTRACTOR, the adopted source extraction program (Bertin & Arnouts 1996, see Section 4.2), had difficulties correcting for. These gradients were found to vary between pointings, so were thought to be caused by diffuse scattered light from bright stars in, or just outside, the observed fields, rather than being the result of vignetting within the instrument. An alternative background subtraction algorithm was developed which computed the background value for every pixel in the image by effectively centring a box (of width 15–25 pixel) on each pixel, calculating the modal value of the background within the box surrounding the central pixel and assigning that value to the central pixel. A bi-cubic spline surface was then fit to the array of modal values in order to create a smoothed sky background map, which was then subtracted from the image.

4 PHOTOMETRY

Initially, photometric zero-points were estimated for each frame in every band for each observing run using the standard star data acquired (see Section 4.1). Using these zero-points, SEXTRACTOR (Bertin & Arnouts 1996) was then used to perform the photometry. After source catalogues had been created for each image (see Section 4.2), accurate photometric zero-points were determined across the V band by comparing objects in overlap regions (see Section 6.1), and adjusting their zero-points relative to a chosen calibrator chip. Finally, the other bands were adjusted relative to the V-band data by comparing the colours of the stars in the ODTS images with those obtained using the Pickles (1998) library of stellar spectra, and applying zero-point corrections needed to match these data sets (see Section 6.2).

4.1 Initial photometric calibration using standard stars

Extracting source counts from the data at this stage will result in a measure of the instrumental magnitude which must be converted to the apparent magnitude. In order to perform this flux calibration, short exposures of various fields containing several standard stars, calibrated by Landolt (1992), were observed through the same filters as target fields of that night. Landolt fields SA92, SA95, SA101 and SA104 covered the ODTS fields well, with several standard stars falling in each frame. For each observing run, at least two of these standard fields were observed and were chosen to span a large airmass range, enabling us to monitor photometric quality throughout the night, and allowing for the subsequent estimation of extinction and colour terms.

As the survey progressed, the large number of non-photometric nights and the substantial overheads associated with multiple-band observations of standard stars prompted the use of an alternative procedure to establish the multiband photometry for each survey region (see Section 6.1). With this method, it is only the zero-pointing of the V-band calibrator chip that is of importance, as the zero-points of the rest of the V-band data are determined by overlap matching (see Section 6.1) and the other bands are then corrected relative to the V band, via stellar locus fitting (see Section 6.2). Data for the Andromeda V-band calibrator frame and the corresponding standard star observations were obtained during photometric conditions, and the zero-point was determined in the usual fashion. The uncertainty on the zero-point of the V-band calibrator frame was found to be 0.07 mag.

4.2 Object extraction using SEXTRACTOR

SEXTRACTOR (Bertin & Arnouts 1996), an automated package, was used to perform the image analysis and source extraction. It is designed for the detection of faint objects in wide-field surveys and so is particularly suited to the ODTS data. It also has the additional advantages of speed, a deblending algorithm and a neural network star–galaxy classifier. As a result of the aforementioned problems with the background subtraction, all images were background subtracted prior to SEXTRACTOR object detection and the background subtraction algorithm used by SEXTRACTOR was switched off.

Convolving the data with a Gaussian filter of full width half maximum (FWHM) close to the seeing is known to optimize detections and reduce noise levels during the source extraction. Hence, a Gaussian filter described by a 3×3 matrix with an FWHM of 1.5–6.1 pixel (0.5–2 arcsec) depending on the seeing, was utilized which had proved, after initial tests, the most effective at faint source extraction. Objects meeting the extraction criteria of having eight connected pixels with flux $>0.4\sigma$ above the local background level were analysed. This corresponded to a minimum of $>1.3\sigma$ per object detection (Booth 2001), however, in practice only $>5\sigma$ detections are included in the final catalogues.

Within SEXTRACTOR, the intensity profile of each source was automatically examined in order to ascertain whether it was a single source or a merged object, where the latter initiates the deblending procedure within SEXTRACTOR. Simulations suggest that photometric errors for objects deblended by SEXTRACTOR are <0.2 mag and in most cases are <0.1 mag. Astrometric errors due to deblending are typically <0.4 pixel (0.1 arcsec) (Bertin & Arnouts 1996).

On occasion, the comparatively low detection threshold used resulted in spurious detections in the wings of both bright and extended objects where the local background noise level was relatively high. Hence the 'cleaning' procedure was implemented within SEXTRACTOR whereby the contribution to the background from bright/extended objects is estimated by fitting them with appropriate Gaussian profiles. Local object intensities remaining above the detection threshold when the adjusted local background was subtracted were accepted into the final catalogue. These spurious detections typically accounted for 10–20 per cent of all detections and those few that remained after cleaning were dealt with during the image masking process detailed in Section 4.4.

SEXTRACTOR was used to calculate aperture and isophotal corrected magnitudes for every source. Aperture magnitudes were obtained by integrating the flux within a fixed aperture and subtracting the contribution from the sky background, its value estimated within

an annulus outside the aperture. For the ODTS, an aperture size of diameter 10 pixel (3.33 arcsec) was used for all bands. Isophotal corrected magnitudes were also computed whereby the flux within a specified isophote, set at 2.5 times the local background level, was integrated. To retrieve flux existing outside the limiting isophote, a Gaussian profile was then fit to the intensity distribution of the object and an estimation of the omitted flux made and subtracted. All extracted magnitudes have an associated rms error calculated within SEXTRACTOR. This random error increases with faintness, but remains small to the limiting depths of the ODTS compared with the various calibration uncertainties (see Section 6.3).

Aperture magnitudes, although consistent, will tend to underestimate the actual magnitude of an extended object due to the flux lost outside the aperture. Simulations suggest that this is negligible for seeing-limited objects fainter than $R \sim 18.5$ in the ODTS data (Olding 2002). Isophotal corrected magnitudes work well for the brighter more extended objects but become unstable at the faint end as they involve assumptions concerning the shapes of objects which become highly uncertain at faint magnitudes. In general, the isophotal corrected magnitudes were found to be less self-consistent than the aperture magnitudes, ascertained by comparing the spread of the ODTS stellar data around the main sequence and the scatter in the difference in magnitudes for common objects found in the overlap regions.

Ultimately, catalogues containing both aperture and isophotal corrected source magnitudes for each frame at each pointing in every band were archived, but aperture magnitudes were used in the final calibrations performed in Section 6, as they give much more consistent colours. Archiving both magnitudes allows the user to choose the magnitude regime most appropriate for their work.

4.3 Star–galaxy separation

During the source extraction, SEXTRACTOR classifies each object as a star or galaxy reflected in the value of the *stellarity index* parameter. A trained neural network was employed to determine the stellarity index for each object dependent on the seeing, peak intensity and a measurement of the isophotal area (see Bertin & Arnouts 1996, for details). The seeing for each pointing was obtained by taking the median FWHM of all bright, unsaturated objects in the image, identified from their profiles as stars. The stellarity index has a value between 0 and 1, where 0 represents a galaxy, 1 a star and intermediate values, by design, give an indication of the uncertainty of the classification. Bertin & Arnouts (1996) claim an algorithm success rate of ≈95 per cent to $R \approx 22$ when the seeing is ≈0.9 arcsec, however, the seeing varies quite dramatically across the ODTS fields. Fig. 6 depicts the behaviour of the stellarity index as a function of magnitude for each band in the Andromeda field. As expected, at faint magnitudes the stellarity index tends towards 0.5 as the distinction between stars and galaxies becomes less pronounced due to object profiles becoming seeing dominated. At very bright magnitudes, the index tends to drop due to saturation effects. From Fig. 6, it is apparent that the classifier begins to break down at magnitudes of $B > 22.5$, $V > 22$, $R > 21.5$ and $I > 21.5$. However, it should be noted that the depths to which the classifier is successful is a strong function of seeing and therefore varies between pointings. All objects with a stellarity index >0.9 were considered to be stars.

4.4 Image masking

False detections caused by the presence of asteroid and satellite trails, excessive vignetting, low-level fringing, diffraction spikes, and haloes around bright stars had to be removed from, or flagged in, the final catalogues. For each image a mask was created manually which identified all the contaminated image areas. The method employed consisted of drawing either rectangular or circular shaped holes around the spurious structures in the data frame, where objects appearing within the holes were then flagged appropriately, allowing for subsequent rejection. An example of an image and its mask can be seen in Fig. 7.

The effective area of the survey was consequently reduced and the final areas for each band in each field after masking are shown in Table 5.

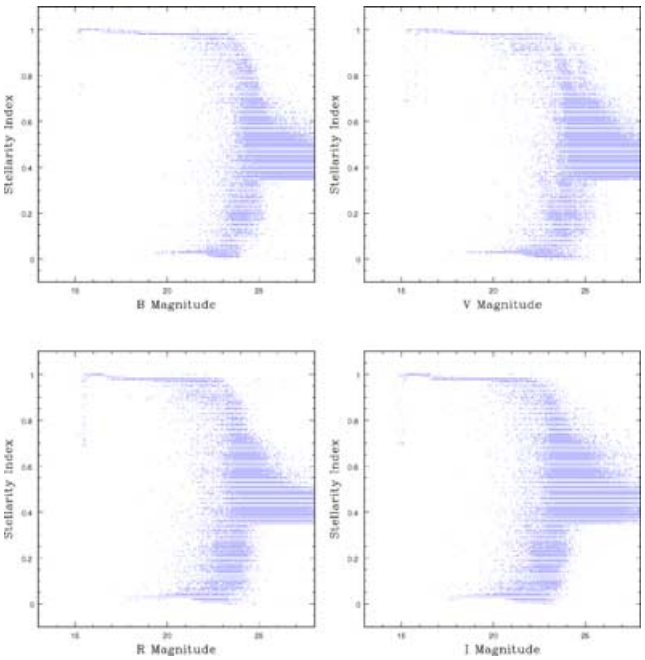

Figure 6. SEXTRACTOR star–galaxy classifier (stellarity index), where 1 represents a star and 0 a galaxy, against magnitude for that of the Andromeda pointings.

5 ASTROMETRY

The conversion of the source pixel position to right ascension α and declination δ was then carried out. The four CCDs of the WFC maintain a fixed geometrical pattern relative to the camera rotator centre, however, the prime focus corrector of the INT introduces a cubic radial distortion term to the plate scale of the form

$$r_{\rm true} = r + kr^3, \tag{1}$$

where $r_{\rm true}$ is the actual radial distance in radians from the field centre, r is the measured radial distance and k is a constant. For the WFC, k was measured to be 220.0 rad^{-2} (Irwin, private communication).

The astrometry is split into two stages. Initially, each individual CCD frame is calibrated independently by roughly matching objects in the images with objects in the corresponding Digitized Sky Survey images (Lasker & Team 1998). Matched objects are then used to converge upon an astrometric fit for each frame via an iterative process. This is performed using the ASTROM package which relates the measured x, y to the true α, δ coordinates by fitting a six coefficient transformation, which includes orientation of the images, plate scale and radial distortions. These fits gave rms residuals of the order of 1 arcsec for each frame. The large residuals were due

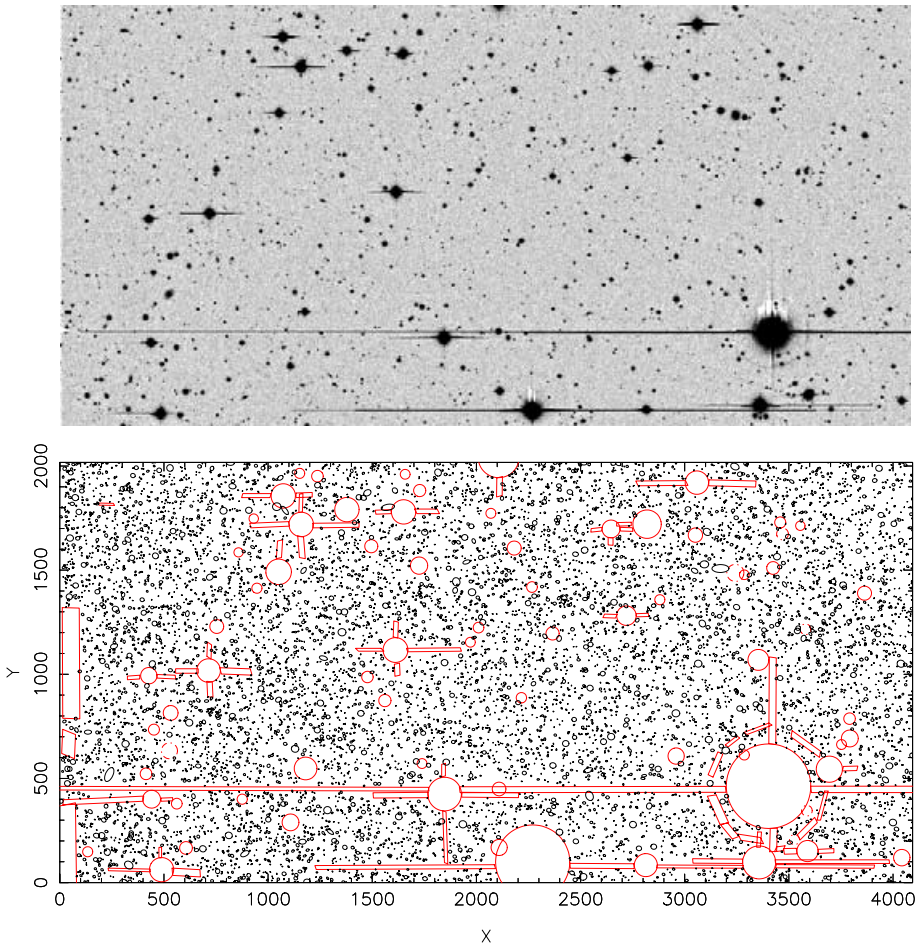

Figure 7. An example of the reduced data (an *R*-band image in Andromeda) and the corresponding image mask created manually to ensure complete removal of all image defects. The black circles in the lower figure represent the extracted sources from the above image, and the red shapes represent the masking out of the bright stars, diffraction spikes and spurious detections appearing at the edge of the chip.

Table 5. Areas of the fully reduced, masked data for each band to date in the ODTS fields.

	Area in deg^2				
Field	*U*	*B*	*V*	*R*	*i*′
Andromeda	0.82	2.16	2.01	2.53	2.23
Lynx	n/a	1.45	1.53	1.50	1.55
Hercules	n/a	0.99	0.58	0.84	1.07

to uncertainties in the exact position of the corrector axis relative to the field rotation centre on the sky.

To compensate for this, the four CCD frames from each pointing were considered as a whole and were matched to the more accurate data of the United States Naval Observatory (USNO) A2.0 astrometric catalogue (Monet 2003). During this matching process, the field centre was allowed to shift using the transformations derived in the initial stage, until the astrometric differences between the ODT and USNO catalogues (see Fig. 8) were minimized, thus ascertaining a more accurate estimate of the true field centre. The final residuals for a single CCD frame were found to be typically $\sim$0.3 arcsec, where Fig. 9 shows an example of the rms residuals for the *V*-band astrometry.

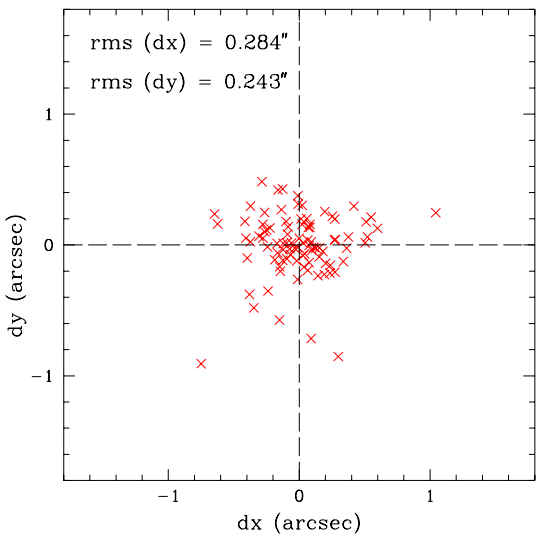

Figure 8. Scatter diagram of the astrometric differences in arcsec between the matched ODT and USNO objects for an example field. The rms differences are small. The pixel size is 0.33 arcsec.

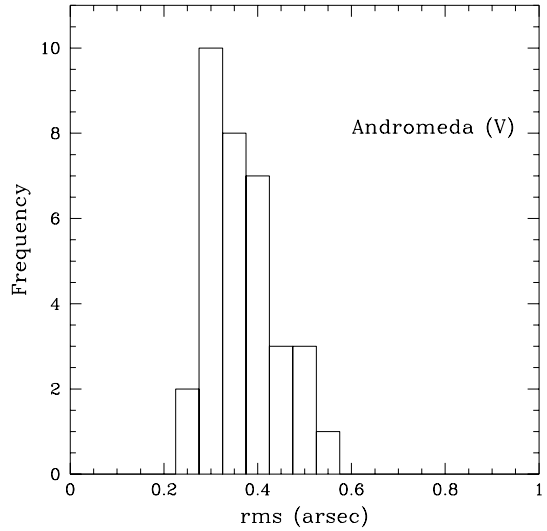

Figure 9. Histogram of the rms astrometric residuals between the ODTS and USNO data found for each individual CCD frame after the final iteration of the astrometric matching procedure for the V-band Andromeda data.

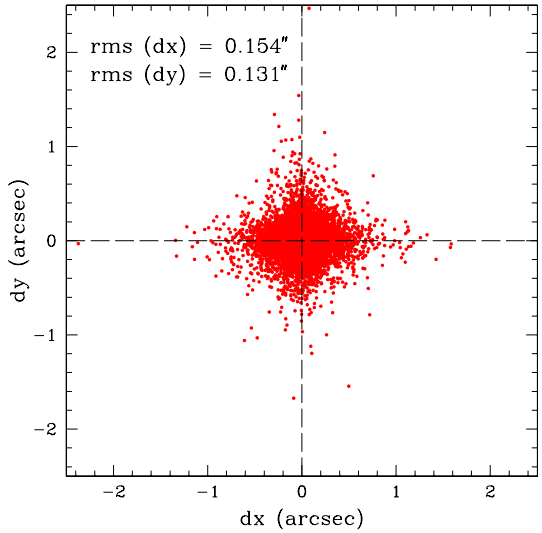

Figure 10. Scatter diagram of the astrometric differences in arcsec between the matched objects in all the overlap regions of the reduced V-band Andromeda data. Objects with $V < 24.5$ have been used so as to avoid using data from overlapping frames which reach different depths.

6 PHOTOMETRIC CALIBRATION

Producing a final catalogue with consistent photometry throughout requires each contiguous field to have a common zero-point. At this stage, the individual zero-points derived in Section 4.1 will each have a residual uncertainty due to differing observing conditions and airmass and extinction variations between observations. Many observations were taken in non-photometric conditions. In order to achieve homogeneity in the photometric calibration, the zero-points of the individual frames must be adjusted relative to a common zero-point adopted for the whole survey. This was carried out in two stages, where the first involved using the V band as the calibrator band (see Section 6.1) and considering the magnitude differences between common objects in the overlap regions of the V-band pointings. The photometric zero-points could then be corrected relative to a chosen calibrator frame, effectively creating a common zero-point across the V-band data. Following this, the zero-points of all the other bands were corrected relative to the V band via stellar locus fitting (see Section 6.2). This was performed by examining the colours of stars in each frame and adjusting their zero-points until the stars had the expected colours of the stellar main sequence.

6.1 Overlap matching

To ensure a common photometric zero-point for the V band, the approach introduced by Glazebrook et al. (1994) was adopted whereby the magnitudes of objects common to overlapping images are compared in order to ascertain the difference in their zero-points. Objects in the overlap regions of adjacent fields were matched with a tolerance of ∼1 arcsec, also a useful check of the astrometric accuracy. Fig. 10 shows the astrometric differences for all the matched objects in the V-band overlap regions, where rms residuals were found to be <0.16 arcsec (with equivalent results for the other bands). If m_i and m_j denote the magnitudes of the matched objects in the overlap regions of frames i and j, then the magnitude offset between overlapping frames, T_{ij}, can be determined by plotting the magnitude differences, $(m_i - m_j)$, against the mean magnitudes, $(m_i + m_j)/2$, for all the objects in the overlap region and making a linear fit to the data to find the average magnitude difference. For the ODTS, the mean magnitude offset was calculated by performing three iterations, after each of which objects deviating by $>1.5\sigma$ from the mean were rejected. A typical example of this is shown in Fig. 11 where 140 objects have been matched, 48 being rejected during the iterative process used to determine the mean. In this particular case, the value of T_{ij} is −0.07 mag with a rms of 0.04.

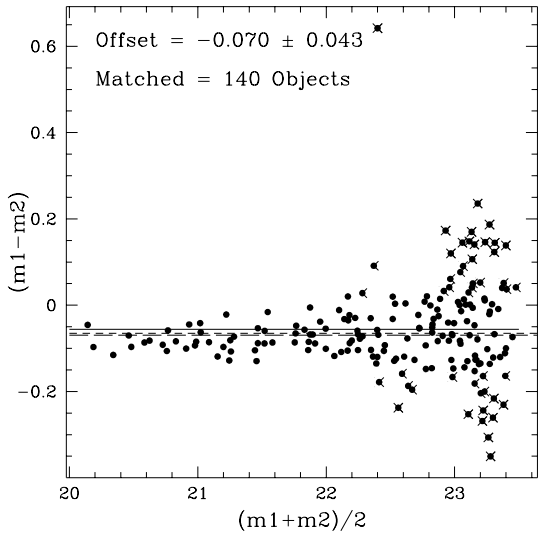

Figure 11. The V-band magnitude (photometric) difference between objects in the overlap region of two adjacent frames plotted against the mean magnitude, where each point represents a matched pair of objects. The three lines represent the value of the mean determined after the first (solid line), second (short broken line) and third (long broken line) iterations of linear fitting to the data, where points deviating from the mean by $>1.5\sigma$ are rejected after each fit (crossed out objects). The magnitude dependence of the photometric errors determined during source extraction is obvious.

If frame i differs from the 'true' zero-point, m_0, so that $m_0 = m_i + C_i$, where C_i is the correction factor for frame i, then the zero-point offset between individual frames can be written

$$T_{ij} = m_i - m_j = C_j - C_i = -T_{ji}. \quad (2)$$

For each frame there will be up to four correction factors corresponding to each of its immediate neighbours. In order to find the best correction, the minimization of the following summation is required,

$$S = \sum_{i=1}^{n} \sum_{j=1}^{n} w_{ij}\theta_{ij}(T_{ij} + C_i - C_j)^2, \tag{3}$$

where n is the number of frames, w_{ij} are the weighting factors $\propto 1/var(T_{ij})$ thus favouring overlaps with small variance and θ_{ij} is the overlap function given by

$$\theta_{ij} = \begin{cases} 1 \text{ if } i \text{ and } j \text{ overlap} \\ 0 \text{ if } i \text{ and } j \text{ do not overlap} \\ 1 \text{ if } i = j. \end{cases}$$

Of the n frames involved, $(1, \ldots, m)$ are, by design, uncalibrated and $(m + 1, \ldots, n)$ are calibrated. For the ODTS, only one frame in the central region of the field was adopted as the calibration frame based on its position, good seeing, photometric conditions during observation, and galaxy number counts. The systematic errors in the plate to plate variations should be (and were) $\leqslant$0.05 mag to avoid introducing artificial large-scale structure (Geller, de Lapparent & Kurtz 1984).

Initially, overlap matching to find a common photometric zero-point was carried out for all bands and it was the V band that was found to possess the smallest scatter in zero-point corrections. This, combined with the V band having the largest coverage, being less likely than B to be affected by variations in both Galactic and atmospheric extinction and being free from fringing effects present in R and i' data justifies the choice of V as the calibrator band.

6.2 Stellar sequence fitting

To calibrate the $UBRi'$ data, the colours of the stellar objects in the ODTS were compared with the expected colours of stars, obtained from the Pickles (1998) stellar library. The model stellar colours were determined by convolving the ODTS spectral response curves (seen in Fig. 1) with the SEDs of the Pickles (1998) sources. Model stellar sequences were derived in six different colour–colour regimes using sixth-order polynomials of the form

$$y = \sum_{j=0}^{n} a_j x^j, \tag{4}$$

where x and y are the chosen colours and a_j are the polynomial coefficients. The best-fitting polynomials are shown in Fig. 12.

Stellar objects were selected from each ODTS frame by choosing stars with $17 < R < 21$ and a star–galaxy classification of $>$0.9 (see Section 4.3). This made use of data with small photometric measurement errors and reliable SEXTRACTOR star–galaxy classification. Any stellar objects lying more that 0.2 mag from the main sequence of objects (in the colour–colour diagrams) were excluded as outliers.

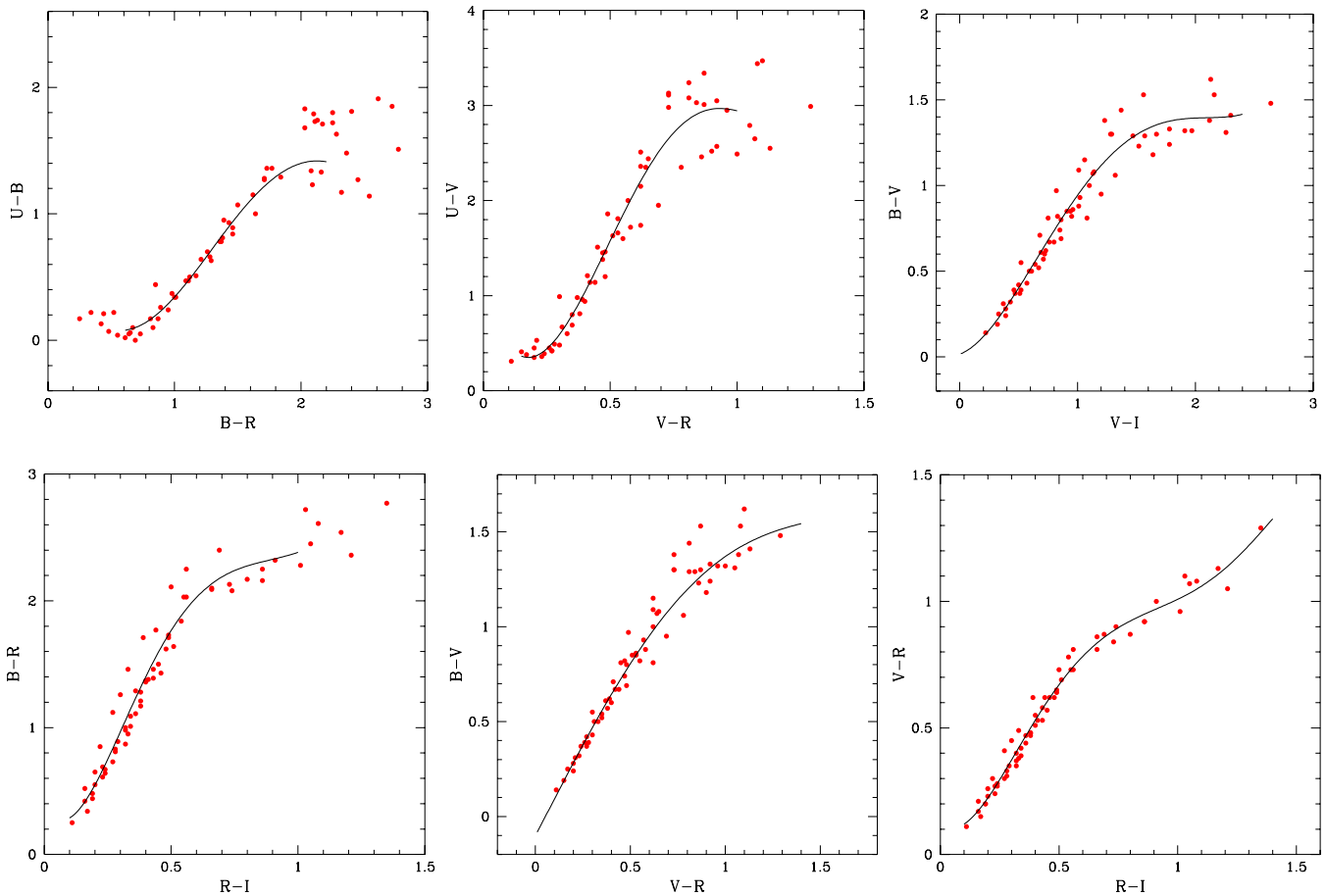

Figure 12. The best-fitting polynomials (black lines) used in the photometric calibration of the ODTS data. Filled red circles represent the colours of Pickles (1998) stellar data in the ODTS filter system, as seen in six different colour–colour planes.

For each frame, in each colour–colour plane shown in Fig. 12, the zero-points were allowed to vary for each of the three colours being examined, with the exception of the V-band zero-point. This remains fixed as V is the chosen calibrator band and the zero-point correction factors for other bands are calculated relative to this. The χ^2 statistic was then computed via

$$\chi^2 = \sum_{i=1}^{N} [y_i - Y(x_i)]^2, \tag{5}$$

where there are N data points with positions x_i and y_i, and $Y(x_i)$ is the value of the best-fitting polynomial (from equation 4) evaluated at x_i. The shifts in x and y that minimize this statistic were computed, as was the final change in colours required for the stellar loci of the ODTS data to match those of Pickles (1998). This process was carried out for all six colour–colour regimes (or four if only $BVRi'$ data were available).

If the zero-point for a given frame in a certain band differs from the 'true' zero-point by a correction factor, C_i, then the measured shifts in colour correspond to the difference between the zero-point correction factors of two different bands, C_i and C_j. Using the same formalization introduced in the previous section, the T_{ij} matrix, which can be solved to find the C_i values for each frame. As the combination of colour–colour regimes constrain the zero-point corrections for each band, the rms scatter in each zero-point determination can be computed from

$$\mathrm{rms} = \frac{\sum_{i=1}^{n}\sum_{j=1}^{n} w_{ij}\theta_{ij}(T_{ij} + Cj - C_i)^2}{\sum_{i=1}^{n}\sum_{j=1}^{n} w_{ij}\theta_{ij}}. \tag{6}$$

Typical rms values were found to be of the order 0.02 mag. An example of the six colour–colour planes showing data before and after correction is shown in Figs 13 and 14. Comparing the $UBRi'$ overlap matches after zero-point corrections were applied gave offsets <0.05 mag suggesting that the photometry is internally consistent at this level.

6.3 Photometric errors

A number of sources of error can affect the photometry. Random errors are estimated during the extraction and measurement of photon counts for an object, and its subsequent conversion to a magnitude. These measurement errors are estimated by SEXTRACTOR for each source extraction. For a typical V-band frame, these errors are <0.025 mag at $V \leqslant 22$, rising to $\sim$0.075 mag by $V \sim 23$ and $\sim$0.3 mag at $V \sim 24.5$. An alternative error estimate was made by plotting the magnitude difference between objects in the overlap region, after photometric calibration, against the average magnitude. This is shown for the V band in Fig. 15, where 2σ error curves have been superimposed. The error estimates given by SEXTRACTOR appear to be systematically lower (by $\approx$0.03 mag) than the errors obtained by examining the photometry of common objects in overlap regions after photometric calibration. This is the case for all the bands.

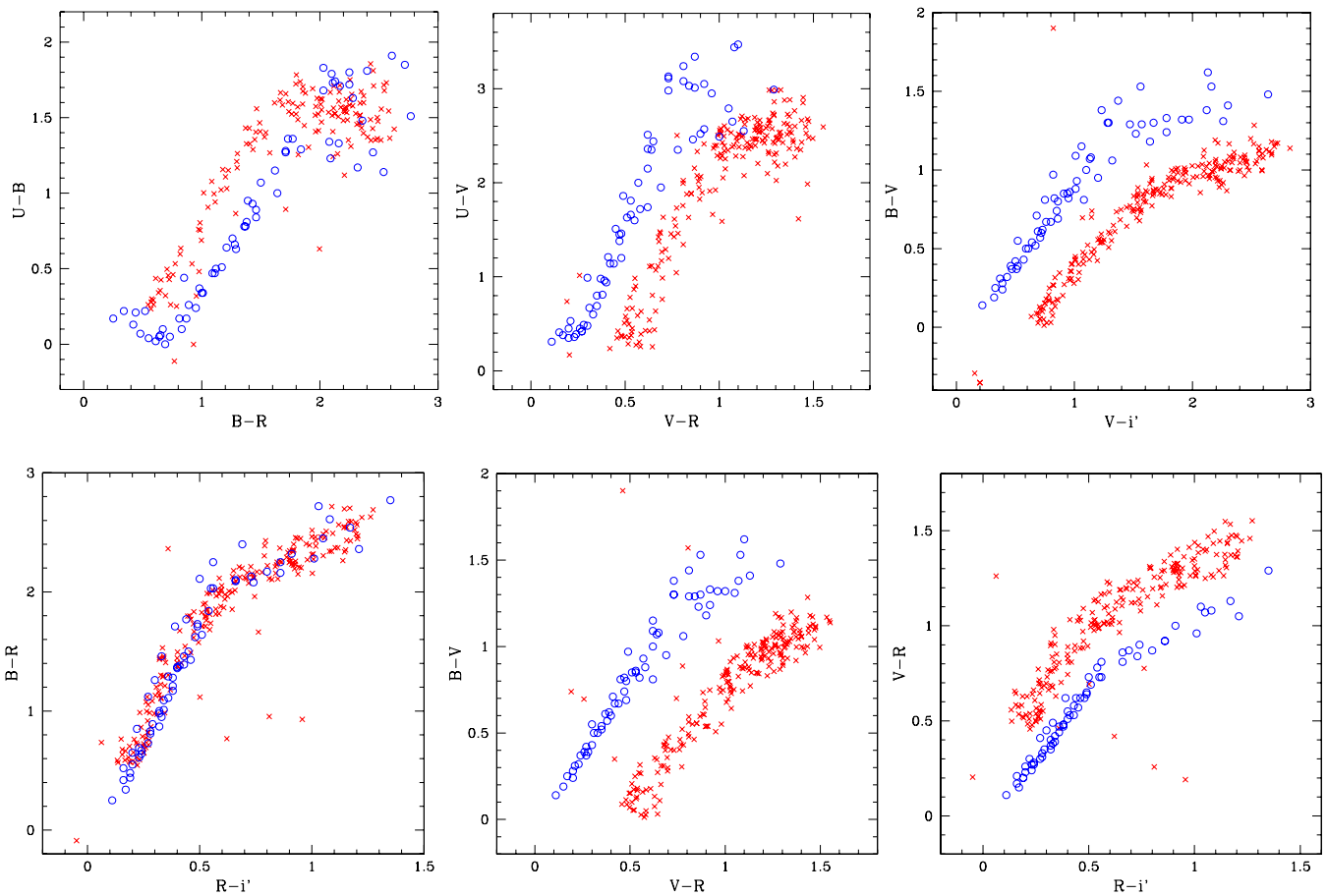

Figure 13. Stellar colours with uncorrected photometric zero-points for an example frame. The open blue circles represent the colours of Pickles (1998) stellar data in the ODTS filter system and the red crosses show the ODTS stellar data. Large initial offsets were expected due to the differing observing conditions.

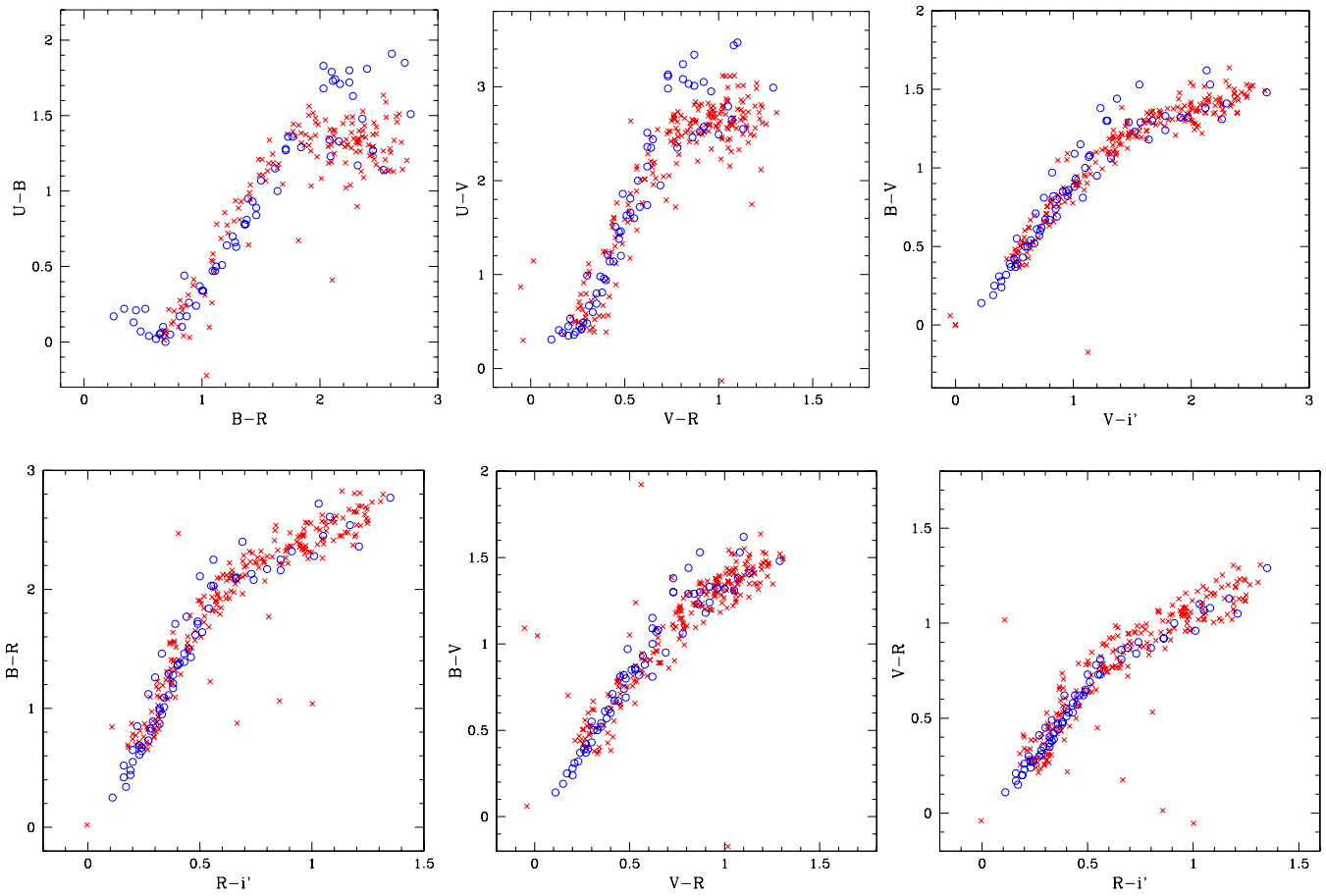

Figure 14. Stellar colours with corrected photometric zero-points for an example frame. The open blue circles represent the colours of Pickles (1998) stellar data in the ODTS filter system and the red crosses show the ODTS stellar data.

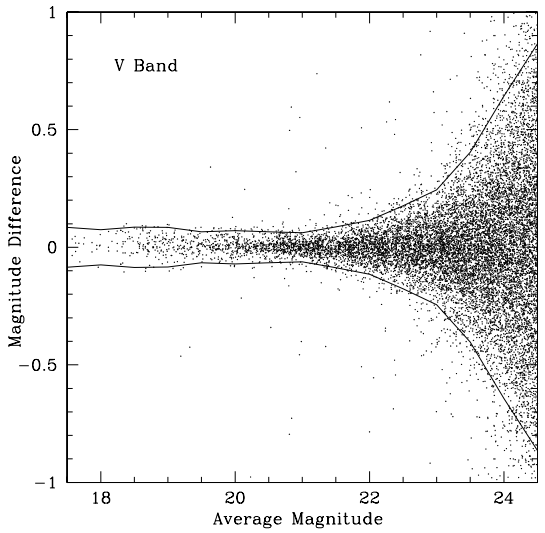

Figure 15. V-band magnitude difference between common objects in overlap regions against the mean magnitude for the reduced Andromeda data after photometric calibration. 2σ error curves have been plotted and objects with $V < 24.5$ have been used so as to avoid using data from overlapping frames which reach different depths.

Two sources of calibration error are introduced during the photometric calibration process; one from the zero-pointing of the V-band mosaic, typically good to $\sim$0.03 mag, and the other from the zero-point calibration of the other bands relative to V using the stellar locus fitting technique, found to introduce errors of $\sim$0.03 mag. Adding these errors in quadrature confirmed that the photometry is *internally consistent* in all bands at the $<$0.05 mag level. A final source of uncertainty comes from the calibration of the V-band data using the photometric standards. The frame used as the calibrator had a zero-point uncertainty of 0.07 mag, resulting in overall photometric uncertainties of $<$0.1 mag.

7 MATCHED CATALOGUE GENERATION

The final catalogues were created by matching the detections within the single colour catalogues to produce one master catalogue for each field, containing magnitudes and errors in all bands, and the corresponding extraction flags.

Routines were constructed to match the single-colour ODTS data using the following approach. All of the astrometric solutions and hole positions were read, along with each of the single colour catalogues. The catalogues were then sorted in turn by right ascension, and matched to the other catalogues using an astrometric tolerance of 3 arcsec. A large array was subsequently produced which contained all the matching information for every object in each filter, and a record of which objects in the other bands they matched. Any inconsistencies arising after the first iteration of the matching routine, e.g. an object deblended by SEXTRACTOR in one filter but not in others due to complex morphology, were isolated and flagged

appropriately. The matching process was then repeated taking account of the new flags. Within the programme, checks were made to establish whether observations in the filter being matched existed, if the object being matched lay within a hole, or if there simply was not a detection in that band. Table 6 gives a list of the flags that were assigned to each detection in the final matched catalogue. The −2 and −3 flags took precedence over the SEXTRACTOR extraction flags unless the SEXTRACTOR flag was >4, which indicates saturation or some sort of extraction problem. Parameters stored for each object included the ODTS identification number, unique to each object and containing information concerning the field, filter, chip number and pixel position, the RA and Dec. coordinates, the SEXTRACTOR star–galaxy classifier, the fluxes, magnitudes, errors in each band and the flags for each band. The final value of the star–galaxy classifier assigned to each object was taken from the data according to the hierarchy *RBVi′KU*, which was so ordered based on the quality, depth and range of the data available. The final matched catalogue produced for the Andromeda field contained ∼1.3 × 10^6 objects.

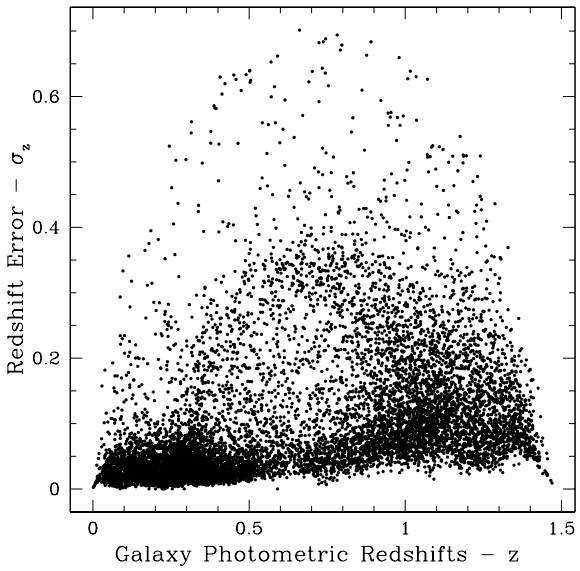

Figure 16. Determined photometric redshifts versus the error in the redshift for a subsection of the matched data from the Andromeda field. All galaxies have $R < 23$ to avoid including fainter galaxies with large photometric errors.

Table 6. Flags used in the matched catalogues determining the reliability of objects or reasons for not matching. The catalogue stores one flag for each filter for every catalogue object.

Flag value	Description
0+	Detected object given its SEXTRACTOR extraction flag
−1	No object detected (but region has been observed)
−2	Object lies in a drilled region (bright star or bad area of the chip
−3	Object lies in a drilled region (bright extended source)
−4	Inconsistent matching, would need follow-up by eye
−8	Region yet to be observed

8 PHOTOMETRIC REDSHIFTS

Photometric redshifts were obtained by comparing the ODTS photometric data with an extensive set of model spectra taken from

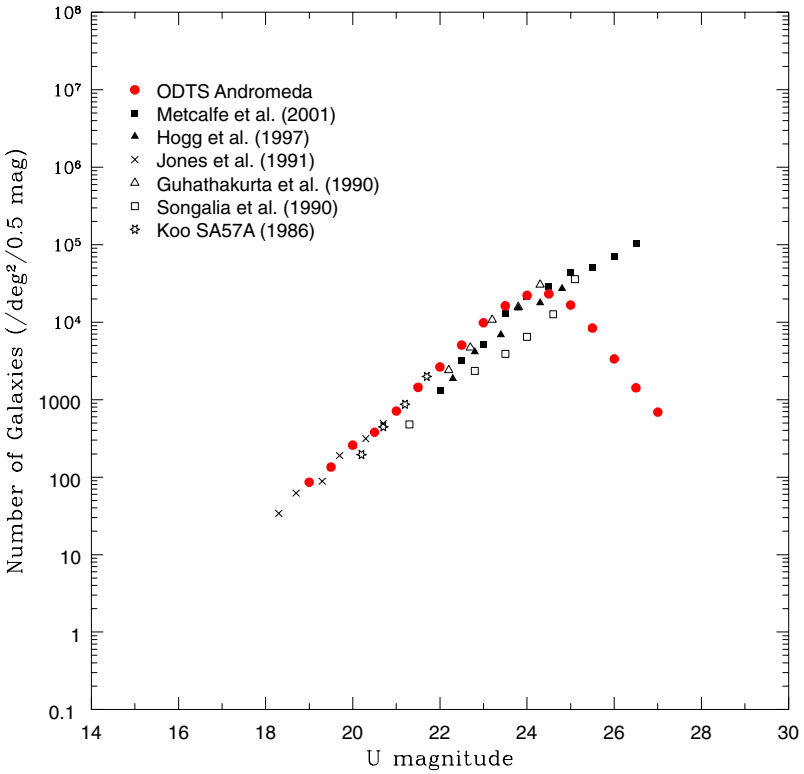

Figure 17. *U*-band galaxy number counts from the ODTS compared with a complication of results taken from various sources. All counts have been converted to the standard photoelectric system. Conversion of the ODTS *U* data to the standard *U* filter (using equation 8) requires matches in *U* and *B*, and consequently the completeness of the *U* data will be dependent of the shallowest depths reached by the matched ODTS *U*- and *B*-band data. Here, *U* is found to be complete to a depth of 24.4. Table 7 presents the data in numerical form.

Table 7. *U*-band number counts for the ODTS, graphed in Fig. 17.

Magnitude	Galaxies 0.5 mag^{-1}	
U	total	deg^{-2}
18.75–19.25	32	86
19.25–19.75	50	135
19.75–20.25	96	259
20.25–20.75	141	380
20.75–21.25	265	714
21.25–21.75	537	1446
21.75–22.25	981	2642
22.25–22.75	1880	5064
22.75–23.25	3651	9834
23.25–23.75	6049	16 290
23.75–24.25	8246	22 210
24.25–24.75	8607	(23 180)
24.75–25.25	6189	(16 670)
25.25–25.75	3115	(8390)
25.75–26.25	1247	(3359)
26.25–26.75	527	(1419)
26.75–27.25	256	(690)

Table 8. *B*-band number counts for the ODTS, graphed in Fig. 18.

Magnitude	Galaxies 0.5 mag^{-1}	
B	total	deg^{-2}
17.75–18.25	17	11
18.25–18.75	27	18
18.75–19.25	74	49
19.25–19.75	135	89
19.75–20.25	204	198
20.25–20.75	286	189
20.75–21.25	548	362
21.25–21.75	1058	699
21.75–22.25	1812	1198
22.25–22.75	2977	1968
22.75–23.25	5131	3392
23.25–23.75	8935	5906
23.75–24.25	15 060	9956
24.25–24.75	22 610	14 940
24.75–25.25	26 890	(17 770)
25.25–25.75	24 050	(15 890)
25.75–26.25	15 680	(10 370)
26.25–26.75	8246	(5451)
26.75–27.25	3745	(2476)

Kinney et al. (1996) galaxy templates, PEGASE stellar synthesis code (Fioc & Rocca-Volmerange 1997), SDSS QSO libraries (Budavari et al. 2001) and the Pickles (1998) stellar templates. Galaxy and QSO models were translated to longer wavelengths, effectively providing comparison spectra over a range of redshifts, and the complete set of templates were then multiplied with the ODTS spectral response functions to obtain potential $U - B$, $B - V$, $V - R$ and $R - I$ colours. The photometric data for each object were then compared with the possible model template colours and likelihoods obtained for each fit. Each object was then classified as a star, galaxy, or QSO, depending on the calculated likelihoods and on the expected number of the three types based on the *I*-band magnitude of the object. The redshift probability distribution was found by summing up

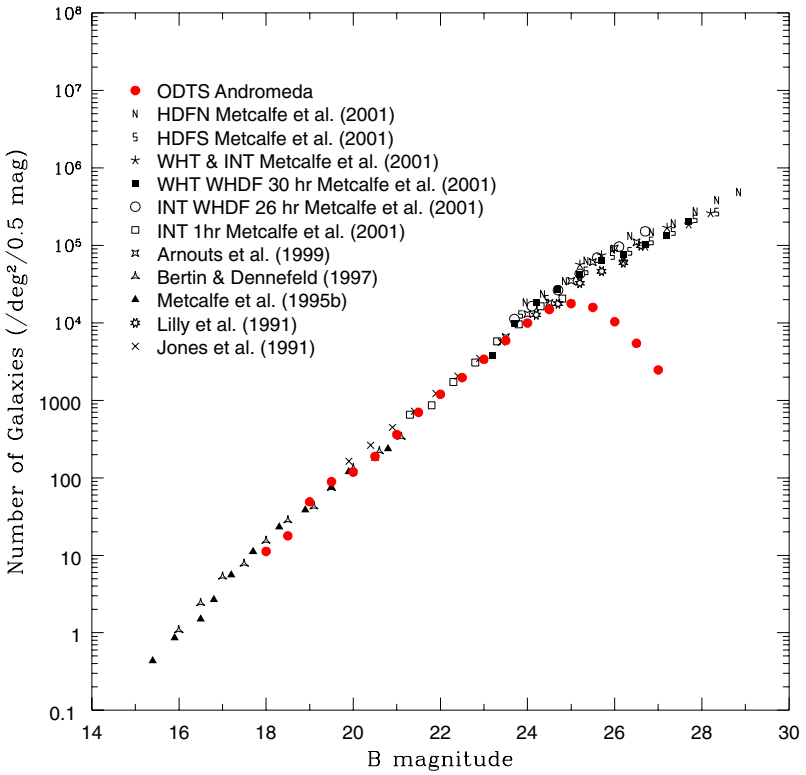

Figure 18. *B*-band galaxy number counts from the ODTS compared with a complication of results taken from various sources. All counts have been converted to the standard photoelectric system. Conversion of the ODTS *B* data to the standard *B* filter (using equation 9) requires matches in *B* and *V*, and consequently the completeness of the *B* data will be dependent of the shallowest depths reached by the matched ODTS *B*- and *V*-band data. Here, *B* is found to be complete to a depth of 25.1. Table 8 presents the data in numerical form.

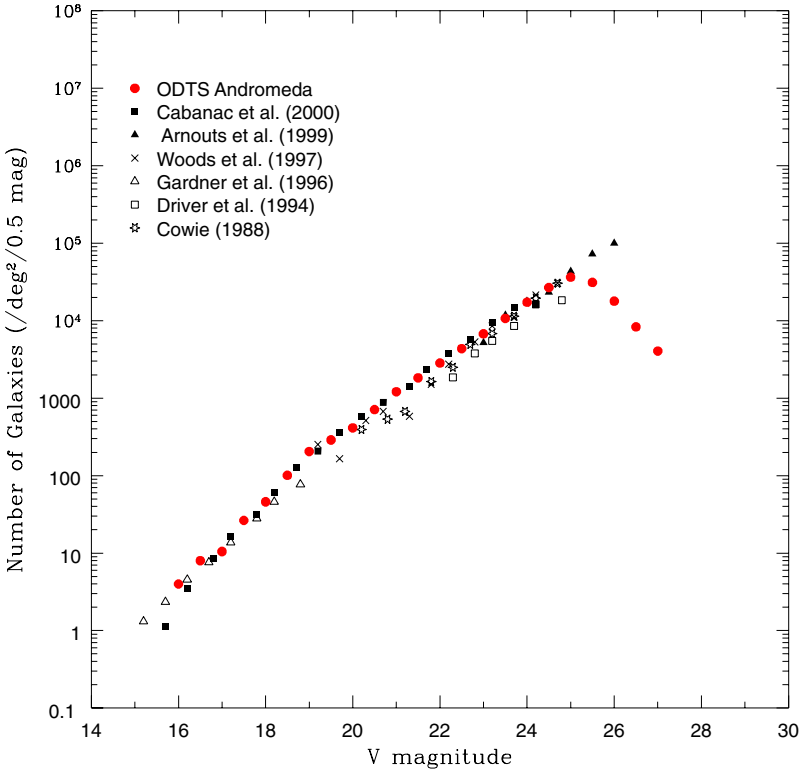

Figure 19. *V*-band galaxy number counts from the ODTS compared with a complication of results taken from various sources. All counts have been converted to the standard photoelectric system. As the Harris *V* filter used in the ODTS is approximately the same as the standard *V* filter, no conversion of the ODTS data was required. Consequently, the completeness of the *V* data will only be dependent on the shallowest depths reached by the ODTS *V* data. Here, *V* is found to be complete to a depth of 24.8. Table 9 presents the data in numerical form.

Table 9. *V*-band number counts for the ODTS, graphed in Fig. 19.

Magnitude	Galaxies 0.5 mag^{-1}	
V	total	deg^{-2}
15.75–16.25	8	4
16.25–16.75	16	8
16.75–17.25	21	11
17.25–17.75	53	26
17.75–18.25	92	46
18.25–18.75	202	101
18.75–19.25	411	205
19.25–19.75	579	289
19.75–20.25	830	414
20.25–20.75	1426	712
20.75–21.25	2430	1213
21.25–21.75	3665	1829
21.75–22.25	5697	2843
22.25–22.75	8745	4364
22.75–23.25	13 540	6756
23.25–23.75	21 470	10 720
23.75–24.25	34 650	17 290
24.25–24.75	53 670	26 780
24.75–25.25	72 940	36 400
25.25–25.75	6240	(31 140)
25.75–26.25	35 850	(17 890)
26.25–26.75	16 660	(8316)
26.75–27.25	8141	(4063)

the maximum likelihoods obtained for all fits to the model SEDs. The redshift error, σ_z, is effectively the standard deviation of the distribution (detailed in Edmondson et al., in preparation). If the source was subsequently classified as a galaxy or QSO then the maximum likelihood redshift determined was recorded, along with the width of the likelihood peak in redshift.

Photometric redshifts were determined for the Andromeda pointings with matched $UBVRi'$ data and Fig. 16 shows the determined redshifts against σ_z for a subsection of this data. Objects were chosen to have $R < 23$ in order to avoid including the fainter objects which have larger associated photometric errors. Within this representative sample, ≈8000 (81 per cent) were found to have $\sigma_z < 0.1$ and ≈6000 to have $\sigma_z < 0.05$ (60 per cent).

An estimate for the median redshift of the ODTS was obtained using the redshift distributions of Fernández-Soto, Lanzetta & Yahil (1999), Cohen et al. (2000), Cowie et al. (2004) and Wirth (2004). From Baugh & Efstathiou (1994), a magnitude dependent redshift distribution can be defined using

$$n(z, R) \propto z^2 \exp - \left[\frac{z}{z_0(R)}\right]^{3/2}, \qquad (7)$$

where $z_0(R) = z_m(R)/1.4$ and $z_m(R)$ is the median redshift as a function of *R*-band magnitude. The $z_m(R)$ is estimated from the redshift distribution of galaxies with known spectroscopic or photometric redshifts sampled in *R*-band magnitude bins of width 0.5 mag. Summing the magnitude dependent model redshift distributions, weighted according to the magnitude distribution of the ODTS, results in an estimate of the redshift distribution for the ODTS, found

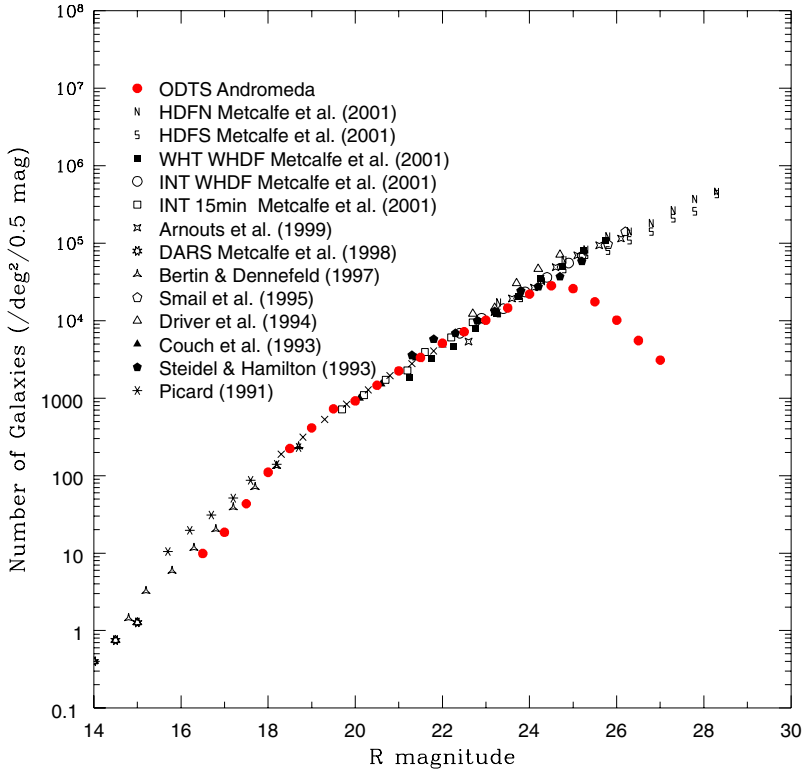

Figure 20. *R*-band galaxy number counts from the ODTS compared with a complication of results taken from various sources. All counts have been converted to the standard photoelectric system. As the Harris *R* filter used in the ODTS is approximately the same as the standard *R* filter, no conversion of the ODTS data was required. Consequently, the completeness of the *R* data will only be dependent on the shallowest depths reached by the ODTS *R* data. Here, *R* is found to be complete to a depth of 24.3. Table 10 presents the data in numerical form.

to be $z_m \approx 0.7$. This was in good agreement with the z_m determined from the median magnitude/median redshift relationship, derived from the COMBO-17 survey, documented in Brown et al. (2003), where the ODTS median *R*-band magnitude of $R_m = 23.2$, corresponds to $z_m \approx 0.7$.

9 GALAXY NUMBER COUNTS

All of the ODTS magnitudes were converted to the standard Johnson–Morgan–Cousins photoelectric filter system, denoted here as *UBVRI*, using the following colour transformation equations[3]

$$U = \frac{(U_{\rm RGO} - B_{\rm KPNO})}{12.167} + U_{\rm RGO} - 0.119, \quad (8)$$

$$B = \frac{(B_{\rm KPNO} - V_{\rm Har})}{7.008} + B_{\rm KPNO} - 0.001, \quad (9)$$

$$I = i'_{\rm Sln} - 0.2006(R_{\rm Har} - i'_{\rm Sln} - 0.004). \quad (10)$$

The Harris *V* and *R* filters used in the ODTS were deemed close enough to the standard photoelectric bands to warrant no conversion. Galaxy number counts for the ODTS are shown in Figs 17, 18, 19, 20 and 21 and are found to be in excellent agreement with previous results. It should be noted that the results shown use *all* of the data from the Andromeda field, thus represent the average depths reached. For a few pointings, where data were acquired in the best conditions, i.e. when the seeing was $\leqslant 1$, the target depths given in Table 2 were reached. For the *V* and *R* bands, where no filter conversions are needed, the depths reached in Figs 19 and 20 depend only on the depths of the ODTS *V* and *R* data, respectively.

[3] See http://www.ast.cam.ac.uk/∼wfcsur/colours.php

Table 10. *R*-band number counts for the ODTS, graphed in Fig. 20.

Magnitude	Galaxies 0.5 mag^{-1}	
R	total	deg^{-2}
16.25–16.75	25	10
16.75–17.25	47	19
17.25–17.75	110	43
17.75–18.25	280	111
18.25–18.75	566	223
18.75–19.25	1049	414
19.25–19.75	1846	729
19.75–20.25	2329	919
20.25–20.75	3706	1463
20.75–21.25	5700	2250
21.25–21.75	8473	3345
21.75–22.25	12 950	5112
22.25–22.75	18 250	7202
22.75–23.25	25 720	10 150
23.25–23.75	37 040	14 620
23.75–24.25	55 750	22 010
24.25–24.75	71 620	(28 270)
24.75–25.25	65 680	(25 930)
25.25–25.75	44 420	(17 540)
25.75–26.25	25 790	(10 180)
26.25–26.75	14 050	(5544)
26.75–27.25	7853	(3100)

However, to enable the conversion of the *U*, *V* and *i*′ ODTS data (as in equations 8–10), only galaxies from the matched catalogue with the necessary multicolour data could be used to derive the galaxy number counts shown. Hence the depths reached in Figs 17, 18 and

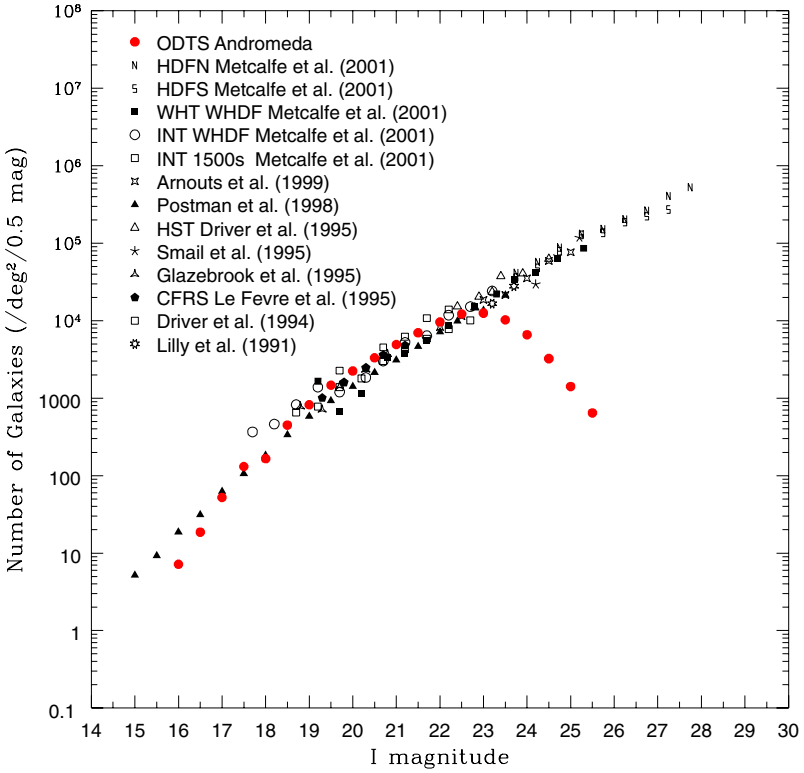

Figure 21. *I*-band galaxy number counts from the ODTS compared with a complication of results taken from various sources. All counts have been converted to the standard photoelectric system. Conversion of the ODTS i' data to the standard *I* filter (using equation 10) requires matches in *R* and i', and consequently the completeness of the *I* data will be dependent of the shallowest depths reached by the matched ODTS *R*- and i'-band data. Here, *I* is found to be complete to a depth of 22.8. Table 11 presents the data in numerical form.

Table 11. *I*-band number counts for the ODTS, graphed in Fig. 21.

Magnitude	Galaxies 0.5 mag^{-1}	
I	total	deg^{-2}
15.75–16.25	10	7
16.25–16.75	26	19
16.75–17.25	73	52
17.25–17.75	183	131
17.75–18.25	231	166
18.25–18.75	628	450
18.75–19.25	1145	820
19.75–20.25	2050	1468
20.25–20.75	3129	2241
20.75–21.25	4634	3319
21.25–21.75	6871	4922
21.75–22.25	9741	6978
22.25–22.75	13 440	9626
22.75–23.25	17 030	12 200
23.25–23.75	17 510	(12 540)
23.75–24.25	14 330	(10 270)
24.25–24.75	9216	(6601)
24.75–25.25	4523	(3240)
25.25–25.75	1978	(1417)

21 will depend on the most shallow of the multiband data used. As a result of this, the depths reached are $U = 24.4$, $B = 25.1$, $I = 22.8$, slightly shallower than the average depths stated in Table 3 which is as expected, $V = 24.8$ and $R = 24.3$, the same depths as those quoted in Table 3.

10 SUMMARY

The Oxford–Dartmouth Thirty Degree Survey is a deep, wide, multiband imaging survey. The Wide Field Camera on the 2.5-m Isaac Newton Telescope on La Palma has been used to obtain $UBVRi'$ data and the *Z*-band data are being acquired using the 2.4-m Hiltner Telescope at the MDM observatory on Kitt Peak. A complementary *K*-band survey is currently being carried out using the 1.3-m McGraw-Hill Telescope at MDM. Four survey regions of 5–10 deg^2, centred at 00:18:24 +34:52 (Andromeda), 09:09:45 +40:50 (Lynx), 13:40:00 +02:30 (Virgo) and 16:39:30 +45:24 (Hercules) have been covered to an average of 5σ limiting depths (Vega) of $B = 25.5$, $V = 25.1$, $R = 24.6$ and $i' = 23.5$, with *U* and *K* subsets covered to depths of 25.1 and 18.5, respectively. Initial data analysis indicates that the ODTS reaches depths ≈0.5 mag shallower than previously anticipated, attributed to less than optimal seeing during observations. On completion of INT observations for the ODTS, approximately 23 deg^2 have been covered in $BVRi'$, with a subset of 1.5 deg^2 in *U*.

This paper details the process from data acquisition, through data reduction and calibration, to the resultant multicolour catalogues.

Photometric redshifts were calculated for a representative sample of objects in the Andromeda field, and were found to have $\sigma_z < 0.1$ for ∼80 per cent of the data and $\sigma_z < 0.05$ for ∼60 per cent of the data. The median redshift of the survey to date was estimated to be $z \approx 0.7$.

Galaxy number counts were determined and were found to compare well with previous survey results.

Preliminary evaluation of the ODTS data shows that the overall quality and quantity of the data is sufficient to meet the initial science objectives of the ODTS. Research undertaken using the ODTS and the results obtained will be documented in the forthcoming papers of this series.

ACKNOWLEDGMENTS

The Isaac Newton Telescope is operated on the island of La Palma by the Isaac Newton Group in the Spanish Observatorio del Roque de los Muchachos of the Instituto de Astrofisica de Canaries. Kitt Peak National Observatory, National Optical Astronomy Observatory, is operated by the Association of Universities for Research in Astronomy, Inc. (AURA) under cooperative agreement with the National Science Foundation. ECM thanks the C. K. Marr Educational Trust. PDA, CEH, EME, and CAB acknowledge the support of PPARC Studentships. This work was supported by the PPARC Rolling Grant PPA/G/O/2001/00017 at the University of Oxford.

REFERENCES

Anderson S.F. et al., 2001, AJ, 122, 503
Arnouts S., D'Odorico S., Cristiani S., Zaggia S., Fontana A., Giallongo E., 1999, A&A, 341, 641
Arnouts S. et al., 2001, A&A, 379, 740
Baugh C.M., Efstathiou G., 1994, MNRAS, 267, 323
Bertin E., Arnouts S., 1996, A&AS, 117, 393
Bertin E., Dennefeld M., 1997, A&A, 317, 43
Booth J., 2001, PhD thesis, Univ. Oxford
Brown M., Taylor A., Bacon D., Gray M., Dye S., Meisenheimer K., Wolf C., 2003, MNRAS, 341, 100
Budavari T., Csabai I., Szalay A. et al., 2001, AJ, 122, 1163
Cabanac R.A., de Lapparent V., Hickson P., 2000, A&A, 364, 349
Cohen J.G., Hogg D.W., Blandford R., Cowie L.L., Hu E., Songaila A., Shopbell P., Richberg K., 2000, ApJ, 538, 29
Colless M. et al., 2001, MNRAS, 328, 1039
Couch W.J., Jurcevic J.S., Boyle B.J., 1993, MNRAS, 260, 241
Cowie L.L., Lilly S.J., Gardner J., McLean I.S., 1988, ApJ, 332, L29
Cowie L., Barger A., Hu E., Capak P., Songaila A., 2004, AJ, submitted
Driver S.P., Phillipps S., Davies J.I., Morgan I., Disney M.J., 1994, MNRAS, 268, 393
Driver S.P., Windhorst R.A., Ostrander E.J., Keel W.C., Griffiths R.E., Ratnatunga K.U., 1995, ApJ, 449, L23
Fernández-Soto A., Lanzetta K.M., Yahil A., 1999, ApJ, 513, 34
Fioc M., Rocca-Volmerange B., 1997, A&A, 326, 950
Gardner J.P., Sharples R.M., Carrasco B.E., Frenk C.S., 1996, MNRAS, 282, L1
Geller M.J., de Lapparent V., Kurtz M.J., 1984, ApJ, 287, L55
Gladders M.D., Yee H.K.C., 2000, AJ, 120, 2148
Glazebrook K., Peacock J.A., Collins C.A., Miller L., 1994, MNRAS, 266, 65
Glazebrook K., Ellis R., Santiago B., Griffiths R., 1995, MNRAS, 275, L19
Guhathakurta P., Tyson J.A., Majewski S.R., 1990, ApJ, 357, L9
Hill G.J., Rawlings S., 2003, New Astron. Rev., 47, 373
Hogg D.W., Pahre M.A., McCarthy J.K., Cohen J.G., Blandford R., Smail I., Soifer B.T., 1997, MNRAS, 288, 404
Jannuzi B.T., Dey A., Brown M.J.I., Tiede G.P., NDWFS Team, 2002, Meeting Am. Math. Soc., 201, 0
Jones L.R., Fong R., Shanks T., Ellis R.S., Peterson B.A., 1991, MNRAS, 249, 481
Kinney A. et al., 1996, ApJ, 467, 38
Koo D.C., 1986, ApJ, 311, 651
Landolt A.U., 1992, AJ, 104, 340
Lasker B.M., Team S.S.-S., 1998, Bull. Am. Astron. Soc., 30, 912
Le Fevre O., Crampton D., Lilly S.J., Hammer F., Tresse L., 1995, ApJ, 455, 60
Lilly S.J., Cowie L.L., Gardner J.P., 1991, ApJ, 369, 79
McCracken H.J., Le Fèvre O., Brodwin M., Foucaud S., Lilly S.J., Crampton D., Mellier Y., 2001, ApJ, 376, 756
Metcalfe N., Fong R., Shanks T., 1995, MNRAS, 274, 769
Metcalfe N., Ratcliffe A., Shanks T., Fong R., 1998, MNRAS, 294, 147
Metcalfe N., Shanks T., Campos A., McCracken H.J., Fong R., 2001, MNRAS, 323, 795
Monet D.G. et al., 2003, AJ, 125, 984
Nonino M. et al., 1999, A&AS, 137, 51
Olding E.J., 2002, PhD thesis, Univ. Oxford
Picard A., 1991, AJ, 102, 445
Pickles A., 1998, Astron. Soc. Pac., San Francisco, Vol. 110, p. 863
Postman M., Lauer T.R., Szapudi I., Oegerle W., 1998, ApJ, 506, 33
Schlegel D.J., Finkbeiner D.P., Davis M., 1998, ApJ, 500, 525
Smail I., Hogg D.W., Yan L., Cohen J.G., 1995, ApJ, 449, L105
Songaila A., Cowie L.L., Lilly S.J., 1990, ApJ, 348, 371
Steidel C.C., Hamilton D., 1993, AJ, 105, 2017
Stoughton C. et al., 2002, ApJ, 123, 485
Wirth G. et al., 2004, preprint, astro-ph/0401353
Wolf C., Meisenheimer K., Rix H.-W., Borch A., Dye S., Kleinheinrich M., 2003, A&A, 401, 73
Woods D., Fahlman G.G., 1997, ApJ, 490, 11

This paper has been typeset from a TEX/LATEX file prepared by the author.